Terrestrial SfM-MVS photogrammetry from smartphone sensors

Stefano Tavani [a,*], Pablo Granado [b], Umberto Riccardi [a], Thomas Seers [c], Amerigo Corradetti [c]

[a] DISTAR, Università degli Studi di Napoli "Federico II", Via Cupa Nuova Cintia, 21, 80126 Napoli, Italy
[b] Institut de Recerca Geomodels, Departament de Dinàmica de la Terra i de l'Oceà, Universitat de Barcelona, Barcelona, Spain
[c] Department of Petroleum Engineering, Texas A&M University at Qatar, Qatar

ARTICLE INFO

Article history:
Received 14 January 2020
Received in revised form 9 June 2020
Accepted 21 June 2020
Available online 23 June 2020

Keywords:
3D model registration
Surveys of cliffs
Camera sensors
GCPs alternative
Remote sensing

ABSTRACT

Smartphones can be regarded as cameras, natively equipped with geolocation and orientation sensors, making them powerful, portable, user-friendly and inexpensive tools for terrestrial structure from motion/multiview stereo photogrammetry (SfM-MVS) surveys. Camera extrinsic parameters (i.e. camera position and orientation), required to produce fully georeferenced SfM-MVS 3D models are available for the majority of smartphone images via inbuilt magnetometer, accelerometer/gyroscope, and global navigation satellite system (GNSS) sensors. The precision of these internal sensors is not yet sufficient to directly use them as input to SfM-MVS photogrammetric reconstructions. However, when the reconstructed scene is significantly greater than the positional error, camera extrinsic parameters can be successfully used to register 3D models during post-processing. We present a survey of a 400 m wide vertical cliff to illustrate a workflow that enables the use of smartphone cameras to generate and fully georeference photogrammetric models without employing ground control points. Survey images were acquired at a distance of ~350 m to the mapped scene using a consumer-grade smartphone. This survey image dataset was subsequently used to build an unreferenced 3D model, which was registered during post-processing using orientation and position metadata tagged to each photograph.

1. Introduction

In many fields within the geosciences, structure from motion/multi-view stereo (SfM-MVS) photogrammetry (e.g. Westoby et al., 2012) has integrated the light detection and ranging (LiDAR) close-range remote sensing technique for the production of decimetre to kilometer scale digital elevation models (DEMs). Typically conducted using only consumer-grade cameras, DEM built from SfM-MVS photogrammetry employs highly portable sensors, which is a key consideration for many applications, such as extraterrestrial field surveys (Caravaca et al., 2019), mapping of caves and mines (e.g. De Waele et al., 2018; Triantafyllou et al., 2019), or in challenging/poorly accessible exposures (Bistacchi et al., 2015; Giuffrida et al., 2020). The low cost of consumer-grade cameras has had a transformative impact upon the uptake of close-range remote sensing within the geosciences, providing an egalitarian approach to DEM generation, which is practically available to all.

The three dimensional (3D) reconstruction and georectification of a scene using digital stereo photogrammetry requires the knowledge of intrinsic and extrinsic camera parameters (e.g. Murtiyoso and Grussenmeyer, 2017 and references therein). The former are either available (in the case of calibrated cameras) or obtainable during post-processing within photogrammetric software (self-calibration), whereas the latter parameters (i.e. the camera location and orientation), are either unavailable or lack sufficient accuracy to be directly used as an input during 3D model reconstruction. This is a particularly crucial issue when acquisition sites are highly collinear, which can often be the case in terrestrial SfM-MVS photogrammetry surveys, especially those mapping quasi-planar exposures. To circumvent this problem, it is common practice to omit extrinsic camera parameters during reconstruction and build an unreferenced and unscaled model within an arbitrary reference frame (e.g. Bemis et al., 2014), and then use the coordinates of at least three non-collinear key-points in the scene (i.e. Ground Control Points, GCPs) to rotate, scale, and translate the model to its real-world position/orientation (e.g. Javernick et al., 2014; James et al., 2017). This procedure might require additional expensive and cumbersome tools, such as multi-frequency Global Navigation Satellite Systems (GNSS) sensors, processed in differential mode, which partially nullifies some of the advantages of SfM-MVS photogrammetry alluded to above. Recently, the possibility of using native orientation sensors within smartphones as an alternative to GCPs to orient unreferenced models, and to evaluate the quality of 3D reconstructions has been explored (Tavani et al., 2019). Here we expand that work, investigating the possibility of using smartphone imagery combined with native GNSS, magnetometer and gyroscope sensors available within most consumer-grade smartphones to produce georectified SfM-MVS models. Current GNSS geotagged smartphone images can be located with a positional accuracy of a few meters or even less (Teunissen and Montenbruck, 2017; Robustelli et al., 2019; Chen et al., 2019).

* Corresponding author.
E-mail address: Stefano.tavani@unina.it (S. Tavani).

Depending on the size of the scene, this level of accuracy can be considered sufficient for many geoscientific applications. For example, hundred meter to few kilometer wide DEMs produced using unmanned aerial vehicles can be successfully registered with GCPs having meter-level accuracy (e.g. Hansman and Ring, 2019). Also, studies seeking to retrieve orientation data from geological structures exposed along cliffs for a variety of applications (e.g. fracture analysis for structural studies or slope stability assessments) require finely oriented 3D models for which absolute position within the geodetic reference frame does not require meter-level accuracy (e.g. Mercuri et al., 2020).

This work aims to demonstrate how orientation and positional information provided by smartphone sensors can be used to build, evaluate, and fully georeference SfM-MVS photogrammetric 3D models without the need to employ GCPs. To do this, we present the results of a smartphone photo-survey of a 400 m wide inaccessible vertical cliff, which has been used to generate a fully georeferenced photogrammetric 3D model of the mapped landform.

2. Methods

The proposed workflow for model building and georeferencing is illustrated in Fig. 1 and includes the following steps.

1. Initially, images of the surveyed scene must be acquired using a smartphone equipped with accelerometer, gyroscope, magnetometer and GNSS sensors. Smartphone images, camera orientation, and image position in a global coordinate system are the only input data within our workflow.
2. Images are used to build an unreferenced model (i.e. having arbitrary scaling, orientation and location) via SfM-MVS photogrammetry in the form of a point cloud. Here, the term 'model' refers to both the reconstructed scene as well as camera position and orientation.
3. Structure from motion estimated camera orientation associated with each image of the unreferenced model ('estimated view direction' from hereafter) is extracted.
4. The estimated view direction of each image is compared with the corresponding image view direction measured by the smartphone ('measured view direction' from hereafter). Rotation parameters (i.e. rotation axis and angle) that are used to match the estimated view directions with the measured view directions are obtained from the estimated and measured camera orientations (Tavani et al., 2019). This also enables the user to distinguish photos whose estimated and measured view directions cannot be successfully matched. This step can be applied recursively, whereby the rotation parameters are recalculated after omitting these outliers.
5. The derived rotation parameters are used to rotate the entire unreferenced model, allowing a correctly oriented 3D model to be obtained.
6. The position of photos in this oriented model (estimated and rotated camera XYZ hereafter) is extracted.
7. Estimated and rotated camera XYZ coordinates are compared with the coordinates registered by the smartphone (measured camera XYZ hereafter), enabling scaling and translation parameters to be derived.
8. Application of the scaling and translation parameters to the model oriented in Step 5 produces a georectified model.

The procedure can be terminated here. However, the following additional optimization steps can also be applied:

9. The X and Y coordinates of the photos in the georectified 3D model are extracted (estimated and rotated-translated-scaled camera XY from hereafter).
10. Estimated and rotated-translated-scaled camera XY are compared with the measured X and Y coordinates, to detect additional rotation around the vertical axis. This is done by aligning the two XY datasets in CloudCompare (version 2.10.1 for Linux).
11. Applying this axial rotation to the model provides the oriented, scaled, centred and finely registered model. This includes both the point cloud and images, whose position should coincide with the measured dataset.

Results of this workflow are compared with an aerial LiDAR DEM, to assess the accuracy of the approach. In detail, after ensuring that no distortion/error occurs in the SfM-MVS model, we trace in 3D the edge of a cliff seen in both the aerial LiDAR and SfM-MVS models. Then, we compare the resulting polylines to detect errors in the georeferencing procedure. As no significant doming effect/scene distortion occurs in the reconstructed model, the correctness of the georeferencing procedure comes down to relative error of the similarity transformation (scaling, translation, rotation) performed on the camera centroids. To evaluate the validity of this transformation, it is not necessary to compare the

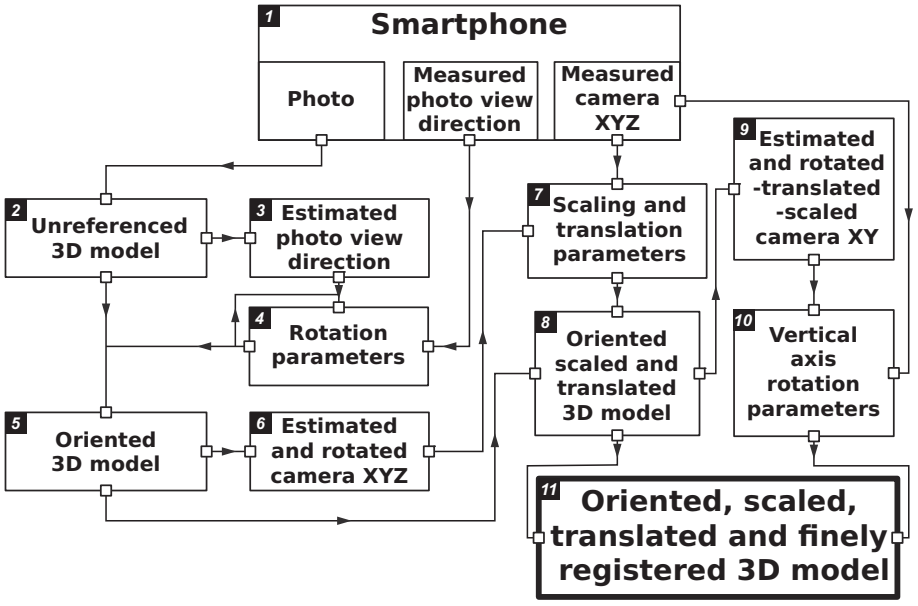

Fig. 1. Workflow for 3D structure from motion/multiview stereo photogrammetry model production and registration from smartphone sensors.

entire model with another 3D model, since the comparison of any 3D object seen in two models is more than sufficient.

3. Data

The SfM-MVS photogrammetric model of a 400 m wide vertical cliff exposed near the Coll de Nargò village, Spain, was constructed using images captured with a Xiaomi MiA1 smartphone (resolution: 12 megapixel/sensor size: 5.11 × 3.84 mm/focal length: 26 mm/35 mm equivalent)/(Fig. 2a). A total of 35 photographs were used in the reconstruction. Images were acquired at a distance of ~350 m from the cliff (Fig. 2b). Positions are expressed in meters (XY in UTM Zone 31N/Z as elevation above sea level; datum WGS84). The XY positioning error, provided by the smartphone itself ranges between 4.5 and 3.2 m (source AngleCam App, see below). Smartphone Z positioning error (ΔZ) is computed by using an aerial LiDAR DEM (datum ETRS89) provided by the Spanish Instituto Geográfico Nacional (http://centrodedescargas.cnig.es/CentroDescargas/; LiDAR 1st coverage 2008–2015). The aerial LiDAR DEM has a ground sampling distance of <1.5 m and an altimetric precision

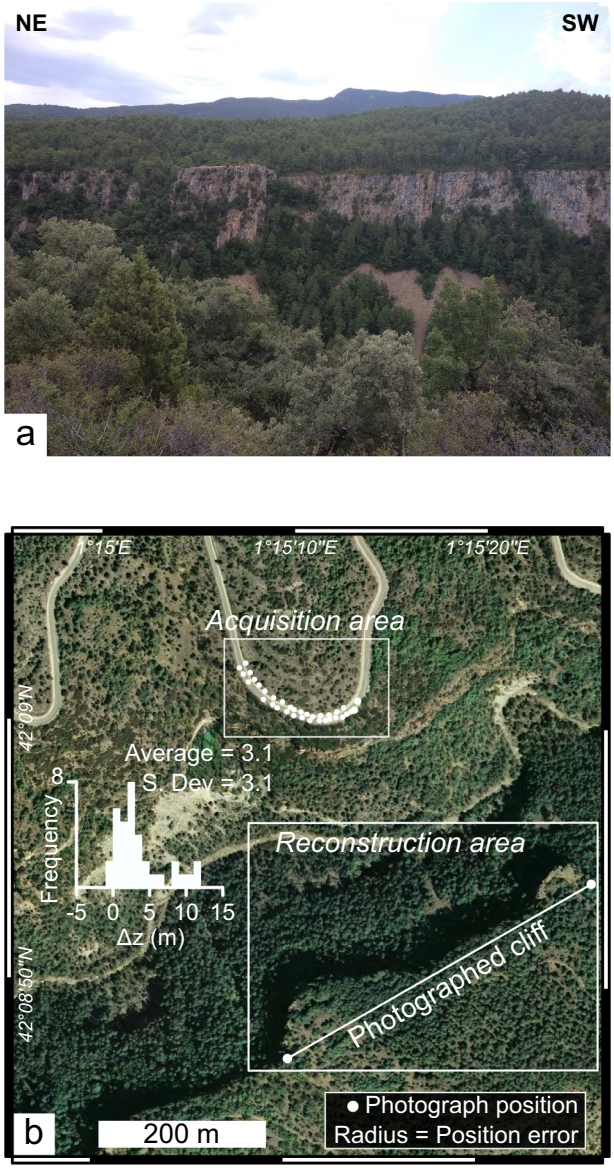

Fig. 2. Input data for the workflow. (A) Photograph of the cliff. (B) Area of investigation with position of the photos and frequency distribution of ΔZ = Z expected in the aerial LiDAR DTM at the photo XY coordinate - Z value provided by the smartphone.

<0.6 m. ΔZ is given by the difference between the altitude of the aerial LiDAR DEM at the given camera XY coordinate and the smartphone measured Z. The frequency distribution of ΔZ is illustrated in Fig. 2b, which shows that Z values provided by the smartphone sensor are on average ~3 m lower than the Z coordinates associated with the reference XY coordinates. It is worth noting that further ~1.7 m must be added to this value, due to the height of the operator, (i.e. there is an average shift of nearly −5 m in the smartphone Z values).

Camera attitude (i.e. the trend and plunge: ~1° and ~0.1° precision respectively) were provided by the AngleCam App for Android OS (version 5.2), which combines data provided by the magnetometer and accelerometer/gyroscope. With respect to the trend of the camera view direction, systematic and random errors are associated with measurements of the magnetic field (e.g. Novakova and Pavlis, 2017; Allmendinger et al., 2017). These errors are sourced by both the sensor itself (i.e. the magnetometer) and the natural variability of the earth's magnetic field, and therefore they cannot be easily accounted for. For this reason, as illustrated below, the georeferencing proposed here only relies on position data, whilst trend data provided by the magnetometer are used only to assess the quality of the model. Data provided by the accelerometer/gyroscope are instead required to constrain the plunge of the view direction, which in turn is a critical input within the model registration procedure. Accordingly, we have conducted an ad hoc stability/accuracy test to compare dip data provided by the smartphone with dip data collected using a Silva compass-clinometer (Supplementary material: Fig. S1). The test evidenced that data provided by the two tools are almost identical, with a discrepancy of 0.6° (±1°).

4. Modelling results

SfM-MVS processing of the Coll de Nargò outcrop photos in Agisoft Metashape (formerly PhotoScan; version 1.5.4 for Linux) resulted in the construction of an unreferenced dense point cloud of ~1.78×10^6 points, covering an area of 90,449 m^2, corresponding to a resolution of ~20 points/m^2.

The view directions of the 35 photos in the model's arbitrary reference frame are presented using stereographic projection in Fig. 3a. Note that in the 'pre-alignment' stereoplot we have indicated the estimated view direction and the measured view direction. Following the procedure described in Tavani et al. (2019), we retrieve the rotation axis and rotation angle to be used to align the estimated view directions to the measured equivalents. The rotation axis, the estimated-and-rotated view directions, and the measured view directions are indicated in the 'aligned' plot within Fig. 3a. After the alignment procedure described above, the quality of the reconstruction can be evaluated by computing the angular difference between the estimated-and-rotated view direction and the measured view direction (Δξ). The frequency distribution of the absolute values of Δξ for the Coll de Nargò outcrop test case is presented in Fig. 3b. Δξ versus location along the survey path (i.e. the normalised distance of each photo from the westernmost photo) and the trend of the measured view directions are shown in Fig. 3c and d respectively. Note that these plots indicate negligible distortion in the model, as Δξ is almost insensitive to the position along the path and the measured view direction. It is worth noting at this point that under these circumstances (i.e. Y not related with X) the R^2 value of the best fit line becomes an irrelevant parameter. However, as shown in Fig. 3b, some photos are characterized by large values of Δξ. Such high values are due to measurement or reconstruction errors, or a combination of both. To evaluate if these photos negatively affect the registration of the model, we removed seven images from the camera orientation dataset, with a threshold for omission being set at Δξ > 4°. Rejection of these low orientation quality images leads to the creation of a new model (Model 2: note that the reconstructed scene remains constant for both models, but the dataset on which the rotation and quality check is computed changes). The rotation axis

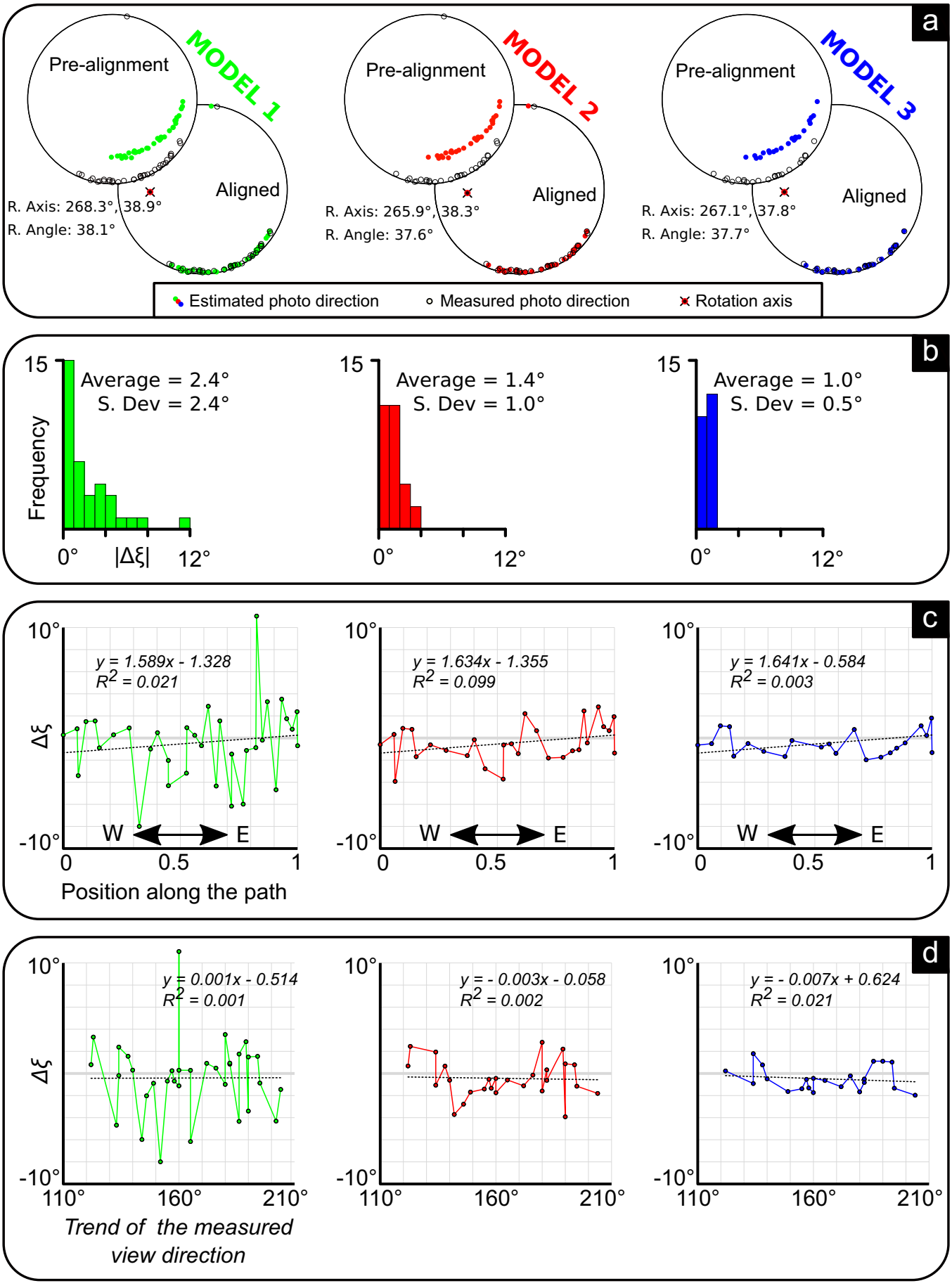
a
Pre-alignment
MODEL 1
Aligned
R. Axis: 268.3°, 38.9°
R. Angle: 38.1°
Pre-alignment
MODEL 2
Aligned
R. Axis: 265.9°, 38.3°
R. Angle: 37.6°
Pre-alignment
MODEL 3
Aligned
R. Axis: 267.1°, 37.8°
R. Angle: 37.7°
Estimated photo direction
Measured photo direction
Rotation axis
b
15
Frequency
Average = 2.4°
S. Dev = 2.4°
0°
|Δξ|
12°
15
Average = 1.4°
S. Dev = 1.0°
0°
12°
15
Average = 1.0°
S. Dev = 0.5°
0°
12°
c
10°
-10°
Δξ
y = 1.589x - 1.328
R2 = 0.021
W
E
0
0.5
1
Position along the path
10°
-10°
y = 1.634x - 1.355
R2 = 0.099
W
E
0
0.5
1
10°
-10°
y = 1.641x - 0.584
R2 = 0.003
W
E
0
0.5
1
d
10°
-10°
Δξ
y = 0.001x - 0.514
R2 = 0.001
110°
160°
210°
Trend of the measured view direction
10°
-10°
y = - 0.003x - 0.058
R2 = 0.002
110°
160°
210°
10°
-10°
y = - 0.007x + 0.624
R2 = 0.021
110°
160°
210°

and angle for Model 2 are only slightly different to those of Model 1 (Fig. 3a). Scatterplots of Δξ versus the position along the survey path and the trend of the measured view direction are comparable to those of Model 1, as indicated by the close values of the best-fit regression lines (Fig. 3c, d). A further model is created at this step (Model 3), by removing six photos having an absolute value of Δξ > 2° from Model 2. Finally, the rotation parameters for Model 3 are assessed (Fig. 3).

The unregistered model built with the entire photographic dataset is rotated using the three rotation axes and angles defined for the three models, producing three oriented 3D models; the three models are then translated and scaled. The translation vector for each model is obtained by aligning the centroid of the GNSS measured camera location dataset to the SfM estimated camera locations. The scaling factor is obtained by dividing the sum of the distances of each photo from the centroid in the measured camera location dataset by the sum of the distances of each photo from the centroid in the estimated and rotated camera XYZ dataset. This procedure can be further optimized by using the estimated and transformed camera XY coordinates. These coordinates are aligned to the measured camera XY coordinates using the alignment function of the CloudCompare software package. This produces the rotation around a vertical axis of the transformed camera locations.

The measured camera XY coordinates and the similarity transformed camera XYZ coordinates for the three models are presented in Fig. 4. For each model, we also provide the frequency distribution of ΔZ and ΔR. As previously described (note that the displayed images have been acquired at 1.7 m above ground level due to the acquisition height of the operator), the true vertical difference between the control and test models (ΔZ) is nearly 5 m. ΔR is the distance in the XY plane between the similarity transformed/optimized camera position and the measured camera position. Both parameters are comparable in the three models, indicating that (i) on average, the reconstructed position is 5 m above the true surface level, and (ii) the horizontal distance between the reconstructed and measured XY position is approximately equal to the smartphone positioning error (i.e. 3.2 to 4.5 m as previously mentioned).

5. Model comparison with aerial LiDAR DEM

Having established the absence of any significant distortion in the reconstructed SfM-MVS model, assessing the quality of the model merely implies assessing the quality of the georeferencing procedure. This is achieved by comparing a morphological feature recognizable in the photogrammetric models with the equivalent feature in the aerial LiDAR control DEM. To achieve this objective, a 0.5 m/px orthophoto is draped onto the aerial LiDAR DEM in MOVE (Petroleum Experts Ltd., version 2019), where we digitize the upper edge of the cliff (Fig. 5a). The cliff is also digitized in the three photogrammetric models directly in Agisoft Metashape (Fig. 5b) and the resultant polylines are imported in MOVE. In Fig. 6 each polyline interpreted from the three photogrammetric datasets is shown in nadir view for comparison with the polyline interpreted from the aerial LiDAR DEM. Projection of each digitized lineament in vertical section is also shown, with the trace of the section being indicated on the map. These maps show that in order to match the two polylines, polylines interpreted from the photogrammetric models must be rotated anticlockwise around a vertical axis by 2.5° (Model 1), 1° (Model 2) and 0.5° (Model 3) respectively. The sections show a vertical shift of polylines interpreted from the photogrammetric models with respect to the aerial LiDAR-derived polyline of 40 m (Model 1), nearly 9 m (Model 2) and 6.4 m (Model 3). These values include both the vertical shift due to the previously described Z translation and disparities in the rotational transform. Given that the distance between the reconstructed scene and surveys stations is nearly 350 m, the rotation component is about 0.6° and 0.2° for Model 2 and 3, respectively, indicating a progressive decrease in errors from Model 1 to Model 3 (i.e. a progressive decrease of errors when omitting cameras with appreciable deviation in estimated orientation of the camera optical axis).

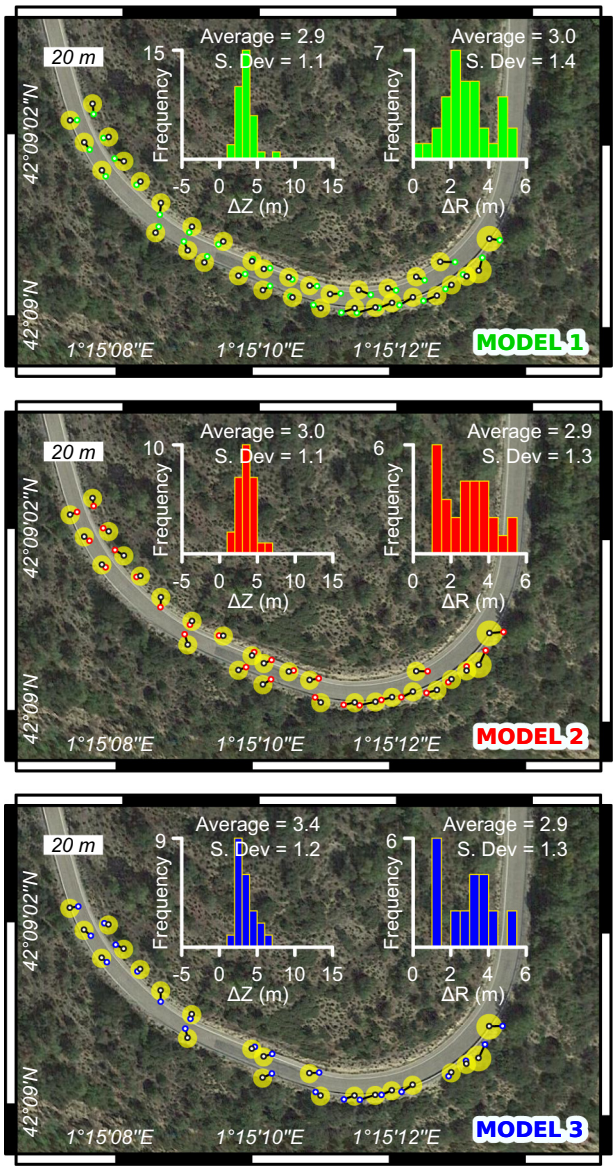

Fig. 4. Reconstructed camera positions after model georeferencing and comparison with measured position. For each model, we show the measured (black circles) and reconstructed (colored) position, with the positioning error provided by the smartphone's internal GNSS sensor (yellow circle). The frequency distribution of ΔZ and ΔR are also provided. ΔZ = Z expected in the aerial LiDAR DEM at the reconstructed camera XY coordinate - Z value provided by the smartphone. ΔR = distance between the measured and reconstructed XY coordinates. Average values and standard deviation of ΔZ and ΔR are also indicated.

Fig. 3. Photo orientation analysis and the models' resultant reconstruction quality assessment. (A) Lower hemisphere stereographic projection of photo's view directions measured with the smartphone and reconstructed in the reference frame of Agisoft Metashape. For each model, the two stereoplots show view direction before and after the alignment. In the 'aligned' stereoplots, the rotation axis and angle are also indicated. (B) Frequency distribution of the absolute difference between the measured and the estimated-and-rotated photo orientation parameters (i.e. Δξ) for the three models. (C) Plots relating Δξ to the normalised position along the survey path for the three models. (D) Plots relating Δξ to the measured view direction for the three models.

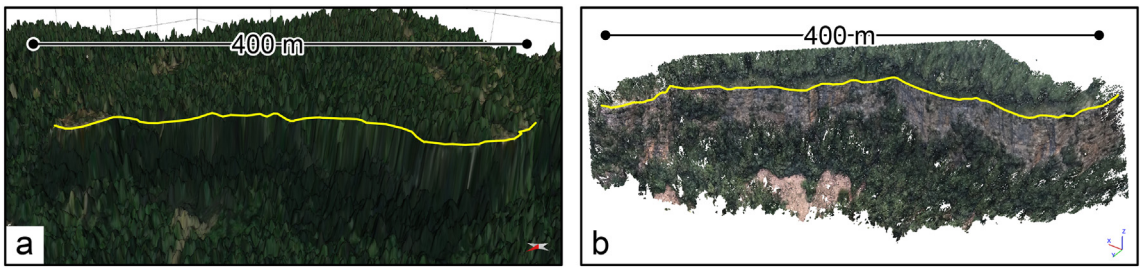

Fig. 5. Digital models of the same cliff used for quality checking. (A) Aerial LiDAR DEM. (B) 3D model constructed using smartphone images. In both models, the edge of the cliff is displayed as a polyline.

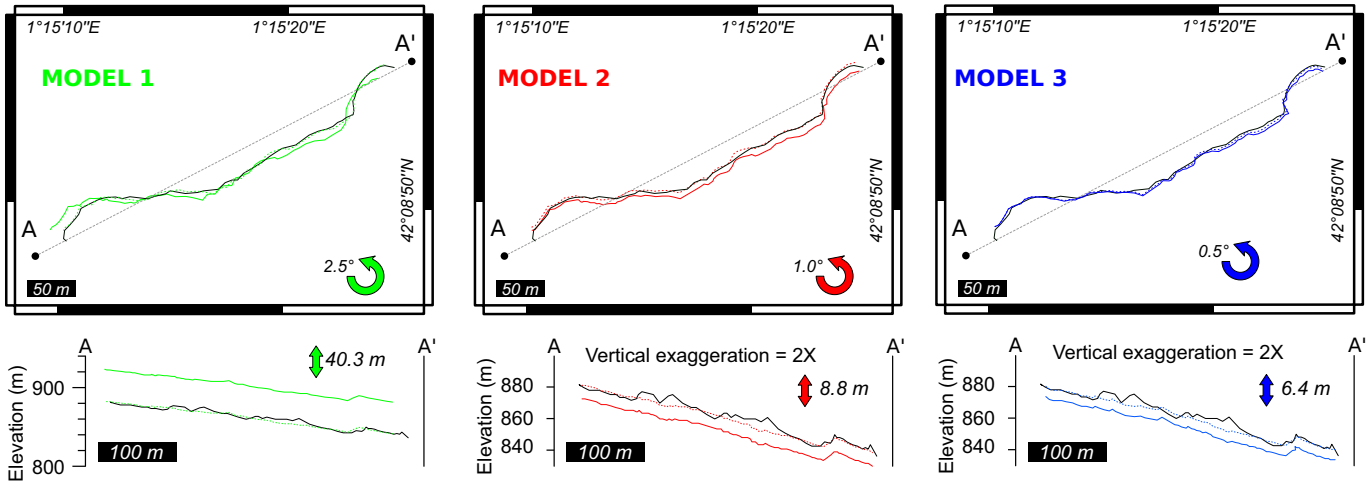

Fig. 6. Comparison between a polyline digitized in the aerial LiDAR DEM (black continuous lines) and in the 3D photogrammetric models (colored continuous lines). For each model, we show the projection of polylines in map view and along a vertical section (the section trace is indicated in the section). Dashed colored lines represent the digitized photogrammetric polylines after rotation around a vertical axis (in map view the rotation angle is indicated) and vertical translation (section: the vertical translation is indicated).

6. Discussion

Over the past decade, smartphone cameras have become increasingly pixel-dense whilst being equipped with progressively larger sensors, allowing to use these devices instead of digital single-lens reflex or mirrorless cameras, for the photo acquisition stage in SfM-MVS photogrammetric reconstruction (e.g. Sofia et al., 2017; Jaud et al., 2019). Here we have used a smartphone, not only to acquire photos but, more importantly, to explore the possibility of using the smartphone sensors for registering the resulting photogrammetric reconstruction.

The first source of error in the proposed workflow relates to geometric distortions in the reconstructed surface emanating from SfM-MVS processing. In SfM-MVS photogrammetric models, gross errors due to erroneous image alignment are easily detectable by visual inspection of the model. However, ostensibly accurate reconstructions still can be affected by errors and, in particular, by the '*doming effect*', which manifests as a scene-wide folding of the reconstructed scene (James and Robson, 2014). Comparison between measured and estimated photo orientation (i.e. assessing the value of $\Delta\xi$) allows doming effects to be detected (Tavani et al., 2019). In cases with negligible doming, $\Delta\xi$ should not relate with the trend of the measured view direction (best-fit linear regression with a slope of ~0°). $\Delta\xi$ versus the position along the survey path is instead characterized by a best-fit linear regression with a slope of 1.6° (Fig. 3). This means that a distortion of 1.6° occurs between the two edges of the photogrammetric outcrop model of the Coll de Nargò case presented in this study, which for a 400 m wide scene can be considered relatively negligible.

The second source of error lies in the smartphone magnetometer and accelerometer/gyroscope, which affect both the computation of $\Delta\xi$ and the final model registration. The trend and plunge of the view direction of the captured photos are provided by the magnetometer and accelerometer/gyroscope respectively, with the initial stage of model registration performed using the aforementioned measurements. However, in our procedure, errors in the measurement of the trend are later tackled by a second registration step (which uses the camera XY coordinates to rotate the model around a vertical axis). Conversely, errors in the measurement of the plunge are not mitigated, and the rotation around the horizontal axis relies entirely on the information provided by the accelerometer/gyroscope. We have shown that the difference between manual dip angle measurements obtained by a Silva compass-clinometer diverges by less than 1° from the measurements obtained by using native smartphone sensors. Moreover, Models 2 and 3 are characterized by rotation around a horizontal axis of less than 0.6°, providing anecdotal confirmation of the robustness of data provided by the accelerometer/gyroscope.

The procedure for registering the model in the post-processing stage is affected by other errors associated with the estimation of camera locations. Specifically, these errors relate to (i) the GNSS positional measurement carried out with the smartphone and (ii) pose estimation during structure from motion photogrammetric reconstruction. Positioning errors affect registration in three ways. Firstly, by introducing discrepancies in each camera centroid. We estimate that this error is <4 m laterally (note that this error is close to the estimated error provided by the GNSS system) and, as detailed above, about 5 m vertically. The second impact relates to the rescaling of the model. An average positioning error of about 4 m for a 200 m long acquisition path implies a maximum admissible scaling error of ~2%. The third issue concerns the rotation around the vertical axis, which in our procedure is constrained by the estimates of lateral camera position provided by the smartphone GNSS: a positioning error of 4 m for the XY coordinates for a 200 m long

acquisition path implies a maximum angular error of 1.4° (i.e. arctangent(4/200)). These maximum errors, however, apply only if the position of photographs in the SfM-MVS photogrammetric model is properly reconstructed for all the photos.

We have shown that incorrectly positioned photos can be recognized by using the Δξ parameter. Omitting cameras with appreciable deviation in estimated orientation of the camera optical axis provides resultant error characteristics in line with the maximum expected errors alluded to above. Model 3 is characterized by rotation about a vertical axis of 0.5°. For this model, the rotation about the horizontal axis coincident to the average photo view direction is zero and the rotation about the horizontal axis perpendicular to the two previous ones is about 0.2°. Scaling errors or lateral shift is not detectable in any of the presented models. Representing the largest error present in the SfM-MVS generated model datasets, a vertical translation of 5 m is, however, readily recognizable, attributable to the single-frequency GNSS sensor.

High-resolution DEMs are the main input data for a variety of geomorphological studies seeking to characterise landforms and Earth surface processes (e.g. Wilson and Gallant, 2000; van Asselen and Seijmonsbergen, 2006). LiDAR sensors and optical cameras equipped on terrestrial and airborne systems permit the production of such high-resolution DEMs. Different combinations of surveying methods and techniques have limitations and advantages, relating to their cost, logistics of operation and achievable resolution, accuracy and precision. Surveys of vast and/or low-relief areas typically require airborne systems (e.g. Székely et al., 2009; Persendt and Gomez, 2016), whereas vertical take-off and landing unmanned aerial vehicles (UAV i.e. drones) are preferred for mapping high-slope areas. However, UAV based photogrammetry has limited flight times (typically <30 min) due to lithium polymer (LiPo) battery duration capacity. Thus, terrestrial surveys offer cost and portability advantages over UAV surveys (e.g. Piermattei et al., 2015), albeit with the disadvantage of a greater propensity for data-shadows and/or scene occlusions where steep cliffs have benches and stepwise geometries. The need of GCPs to georeference SfM-MVS photogrammetric models partially nullifies some of the advantages of terrestrial SfM-MVS photogrammetry. In particular, the portability of GNSS sensors used to retrieve the position of GCPs, along with the necessity of physical placement of GCPs within the scene may represent critical limitations. Here, we have shown that both issues can be addressed using smartphone's cameras, to produce terrestrial SfM-MVS photogrammetry models that can be fully georectified using data provided by the smartphone's GNSS, accelerometer/gyroscope and magnetometer sensors. The main limitations of the proposed procedure are: (1) low-relief landforms or horizontal outcrops cannot be reconstructed and (2) there is an appropriate scale for which this approach can be used. Apart from the photo ground sampling distance (controlling the maximum theoretical resolution of SfM-MVS photogrammetry models), the scale of the reconstructed scene is determined by the ratio between the accuracy of the smartphone's GNSS sensor and the width of the scene/acquisition area. In this sense, we have shown that satisfactory georeferencing can be achieved only when positioning error is less than 1–2% of the width of the acquisition area/reconstructed scene. In essence, the proposed method can be particularly useful for the mapping and monitoring of high-relief slope landforms such as wide rocky cliffs or banks of incised valleys.

7. Conclusions

In this work we have proposed a novel workflow that utilizes consumer-grade smartphone sensors to produce fully georeferenced SfM-MVS surface reconstructions of large-scale (i.e. a few hundred meters to several kilometers wide) scenes. Information provided by the GNSS, accelerometer/gyroscope and magnetometer allows registering 3D surface reconstructions obtained by SfM-MVS image processing toolchains, without the need for GCPs, provided the doming effect of the SfM-MVS photogrammetric reconstruction is negligible and that the reconstructed scene is considerably larger than the mean GNSS error. The proposed workflow allows geoscience practitioners to produce georectified 3D models whilst eliminating the need for expensive and cumbersome positioning tools. For several hundred-meter-wide scenes, the error is negligible in terms of scaling and positioning, whereas rotations of less than 1° about vertical and horizontal axes can be routinely attained.

Declaration of competing interest

The authors declare that they have no known competing financial interests or personal relationships that could have appeared to influence the work reported in this paper.

Acknowledgements

Comments from two anonymous reviewers benefited the final version of this contribution. The Institut de Recerca Geomodels acknowledges funding from 2014SGR467SGR.

References

Agisoft Metashape [Software], d. https://www.agisoft.com/.

Allmendinger, R.W., Siron, C.R., Scott, C.P., 2017. Structural data collection with mobile devices: accuracy, redundancy, and best practices. J. Struct. Geol. 102, 98–112. https://doi.org/10.1016/j.jsg.2017.07.011.

AngleCam App [Software], d. http://anglecam.derekr.com.

Bemis, S.P., Micklethwaite, S., Turner, D., James, M.R., Akciz, S., Thiele, S.T., Bangash, H.A., 2014. Ground-based and UAV-based photogrammetry: a multi-scale, high-resolution mapping tool for structural geology and paleoseismology. J. Struct. Geol. 69, 163–178. https://doi.org/10.1016/j.jsg.2014.10.007.

Bistacchi, A., Balsamo, F., Storti, F., Mozafari, M., Swennen, R., Solum, J., Tueckmantel, C., Taberner, C., 2015. Photogrammetric digital outcrop reconstruction, visualization with textured surfaces, and three-dimensional structural analysis and modeling: innovative methodologies applied to fault-related dolomitization (Vajont Limestone, Southern Alps, Italy). Geosphere 11, 2031–2048. https://doi.org/10.1130/GES01005.1.

Caravaca, G., Le Mouélic, S., Mangold, N., L'Haridon, J., Le Deit, L., Massé, M., 2019. 3D digital outcrop model reconstruction of the Kimberley outcrop (Gale crater, Mars) and its integration into virtual reality for simulated geological analysis: Planet. Space Sci. 104808. doi:https://doi.org/10.1016/j.pss.2019.104808

Chen, B., Gao, C., Liu, Y., Sun, P., 2019. Real-time precise point positioning with a Xiaomi MI 8 android smartphone. Sensors 19, 2835. https://doi.org/10.3390/s19122835.

CloudCompare [Software], d. https://www.danielgm.net/cc/.

De Waele, J., Fabbri, S., Santagata, T., Chiarini, V., Columbu, A., Pisani, L., 2018. Geomorphological and speleogenetical observations using terrestrial laser scanning and 3D photogrammetry in a gypsum cave (Emilia Romagna, N. Italy). Geomorphology 319, 47–61. https://doi.org/10.1016/j.geomorph.2018.07.012.

Giuffrida, A., Agosta, F., Rustichelli, A., Panza, E., La Bruna, V., Eriksson, M., Torrieri, S., Giorgioni, M., 2020. Fracture stratigraphy and DFN modelling of tight carbonates, the case study of the Lower Cretaceous carbonates exposed at the Monte Alpi (Basilicata, Italy). Mar. Pet. Geol. 112, 104045. https://doi.org/10.1016/j.marpetgeo.2019.104045.

Hansman, R.J., Ring, U., 2019. Workflow: from photo-based 3-D reconstruction of remotely piloted aircraft images to a 3-D geological model. Geosphere 15, 1393–1408. https://doi.org/10.1130/GES02031.1.

James, M.R., Robson, S., 2014. Mitigating systematic error in topographic models derived from uav and ground-based image networks. Earth Surf. Process. Landforms 39, 1413–1420. https://doi.org/10.1002/esp.3609.

James, M.R., Robson, S., D'Oleire-Oltmanns, S., Niethammer, U., 2017. Optimising UAV topographic surveys processed with structure-from-motion: ground control quality, quantity and bundle adjustment. Geomorphology 280, 51–66. https://doi.org/10.1016/j.geomorph.2016.11.021.

Jaud, M., Kervot, M., Delacourt, C., Bertin, S., 2019. Potential of smartphone SfM photogrammetry to measure coastal morphodynamics. Remote Sens. 11, 2242. https://doi.org/10.3390/rs11192242.

Javernick, L., Brasington, J., Caruso, B., 2014. Modeling the topography of shallow braided rivers using structure-from-motion photogrammetry. Geomorphology 213, 166–182. https://doi.org/10.1016/j.geomorph.2014.01.006.

Mercuri, M., McCaffrey, K.J., Smeraglia, L., Mazzanti, P., Collettini, C., Carminati, E., 2020. Complex geometry and kinematics of subsidiary faults within a carbonate-hosted relay ramp. J. Struct. Geol. 130, 103915. https://doi.org/10.1016/j.jsg.2019.103915.

MOVE 2019 [Software], d. http://www.petex.com/products/move-suite/.

Murtiyoso, A., Grussenmeyer, P., 2017. Documentation of heritage buildings using close-range UAV images: dense matching issues, comparison and case studies. Photogramm. Rec. 32, 206–229. https://doi.org/10.1111/phor.12197.

Novakova, L., Pavlis, T.L., 2017. Assessment of the precision of smartphones and tablets for measurement of planar orientations: a case study. J. Struct. Geol. 97, 93–103. https://doi.org/10.1016/j.jsg.2017.02.015.
Persendt, F.C., Gomez, C., 2016. Assessment of drainage network extractions in a low-relief area of the Cuvelai Basin (Namibia) from multiple sources: LiDAR, topographic maps, and digital aerial orthophotographs. Geomorphology 260, 32–50. https://doi.org/10.1016/j.geomorph.2015.06.047.
Piermattei, L., Carturan, L., Guarnieri, A., 2015. Use of terrestrial photogrammetry based on structure-from-motion for mass balance estimation of a small glacier in the Italian alps. Earth Surf. Process. Landforms 40, 1791–1802. https://doi.org/10.1002/esp.3756.
Robustelli, U., Baiocchi, V., Pugliano, G., 2019. Assessment of dual frequency GNSS observations from a Xiaomi Mi 8 android smartphone and positioning performance analysis. Electronics 8, 91. https://doi.org/10.3390/electronics8010091.
Sofia, G., Masin, R., Tarolli, P., 2017. Prospects for crowdsourced Information on the geomorphic 'engineering' by the Invasive Coypu (Myocastor coypus). Earth Surf. Process. Landforms 42, 365–377. https://doi.org/10.1002/esp.4081.
Székely, B., Zámolyi, A., Draganits, E., Briese, C., 2009. Geomorphic expression of neotectonic activity in a low relief area in an airborne laser scanning DTM: a case study of the Little Hungarian Plain (Pannonian Basin). Tectonophysics 474, 353–366. https://doi.org/10.1016/j.tecto.2008.11.024.
Tavani, S., Corradetti, A., Granado, P., Snidero, M., Seers, T.D., Mazzoli, S., 2019. Smartphone: an alternative to ground control points for orienting virtual outcrop models and assessing their quality. Geosphere 15, 2043–2052. https://doi.org/10.1130/GES02167.1.
Teunissen, P.J.G., Montenbruck, O., 2017. Springer Handbook of Global Navigation Satellite Systems. Springer International Publishing, Cham https://doi.org/10.1007/978-3-319-42928-1.
Triantafyllou, A., Watlet, A., Le Mouélic, S., Camelbeeck, T., Civet, F., Kaufmann, O., Quinif, Y., Vandycke, S., 2019. 3-D digital outcrop model for analysis of brittle deformation and lithological mapping (Lorette cave, Belgium). J. Struct. Geol. 120, 55–66. doi: doi:https://doi.org/10.1016/j.jsg.2019.01.001
van Asselen, S., Seijmonsbergen, A.C., 2006. Expert-driven semi-automated geomorphological mapping for a mountainous area using a laser DTM. Geomorphology 78, 309–320. https://doi.org/10.1016/j.geomorph.2006.01.037.
Westoby, M.J., Brasington, J., Glasser, N.F., Hambrey, M.J., Reynolds, J.M., 2012. 'Structure-from-motion' photogrammetry: a low-cost, effective tool for geoscience applications. Geomorphology 179, 300–314. https://doi.org/10.1016/j.geomorph.2012.08.021.
Wilson, J.P., Gallant, J.C., 2000. Terrain Analysis. Principles and Applications. John Wiley & Sons, Inc., Chichester.